Analytical solution for diverging elliptic shear wave in bounded and unbounded transverse isotropic viscoelastic material with nonhomogeneous inner boundary

Martina Guidetti and Thomas J. Royston

Citation: The Journal of the Acoustical Society of America **145**, EL59 (2019); doi: 10.1121/1.5088028
View online: https://doi.org/10.1121/1.5088028
View Table of Contents: https://asa.scitation.org/toc/jas/145/1
Published by the Acoustical Society of America

Martina Guidetti and Thomas J. Royston: JASA Express Letters https://doi.org/10.1121/1.5088028 Published Online 24 January 2019

Analytical solution for diverging elliptic shear wave in bounded and unbounded transverse isotropic viscoelastic material with nonhomogeneous inner boundary

Martina Guidetti and Thomas J. Royston[a)]
Richard and Loan Hill Department of Bioengineering, 851 South Morgan Street, MC 063, University of Illinois at Chicago, Chicago, Illinois 60607, USA
troyston@uic.edu, mguide2@uic.edu

Abstract: A theoretical approach was recently introduced by Guidetti and Royston [J. Acoust. Soc. Am. **144**, 2312–2323 (2018)] for the radially converging elliptic shear wave pattern in transverse isotropic materials subjected to axisymmetric excitation normal to the fiber axis at the outer boundary of the material. This approach is enabled via a transformation to an elliptic coordinate system with isotropic properties. The approach is extended to the case of diverging shear waves radiating from a cylindrical rod that is axially oscillating perpendicular to the axis of isotropy and parallel to the plane of isotropy.

Date Received: October 15, 2018 **Date Accepted:** January 4, 2019

1. Introduction

Please refer to the authors' recent publication in this journal[1] for an extensive summary of the background and motivation for the coordinate transformation strategy extended in the present article to the case of a radially diverging shear wave front caused by an oscillating rod at the center.

Continuous oscillatory motion of a cylindrical rod along its axis generates diverging shear waves in an unbounded medium or in one where back reflections from boundaries are negligible or directionally filtered out, and can establish a standing wave pattern in a bounded cylindrical region. This strategy has been applied *in vivo* with complex organ and tissue boundaries[2–4] and *in vitro* on tissue specimens or phantoms confined to cylindrical containers.[5–8] Additionally, application of focused radiation force of ultrasound (US), commonly used in US-based dynamic elastography methods, may be roughly approximated as a rod-like source oscillating along its axis.[9–11] While a theoretical solution for the axisymmetric shear wave pattern that is established in isotropic materials is easily obtained using Bessel functions, a solution for the case of anisotropic materials that will produce a nonaxisymmetric shear wave pattern is not as easily found. Specifically, to the best of the authors' knowledge such a closed form theoretical solution has not been presented and validated for the case of a transverse isotropic material that is aligned with its plane of isotropy parallel to the oscillating rod. Such a configuration should result in the generation of only slow shear waves whose phase propagation speed will depend on the angle their direction of propagation makes with the plane of isotropy.

A theoretical approach is proposed for the elliptic shear wave pattern observed in transverse isotropic materials subjected to axisymmetric excitation parallel to the plane of isotropy. Radially diverging waves driven by axial oscillation of a rigid cylindrical rod located at the center of a bounded cylindrical region or radiating into an unbounded region are considered. The theoretical solutions are validated via numerical finite element analysis (FEA) case studies.

2. Theory

Please refer to Sec. II A of Ref. 1 for an introduction to the nomenclature and equations used for nearly incompressible isotropic linear viscoelastic material, and for an orientation to the geometry considered in this study. In the present study the outer boundary at $r = r_0$ is fixed and there is a rod of radius $r = r_i$ along the central axis of the cylindrical phantom as shown in Fig. 1. One means of creating steady state

a)Author to whom correspondence should be addressed.

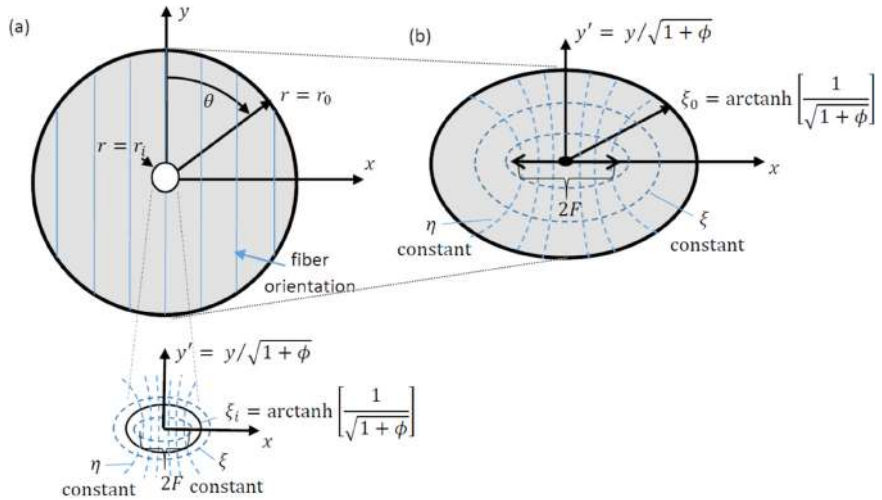

Fig. 1. (Color online) Transverse isotropic cylindrical sample with x-z plane of isotropy (fibers in the y direction) subjected to a nonhomogeneous boundary condition: harmonic displacement in the z direction of amplitude u_{zr_i} at frequency $f = \omega/2\pi$ on its curved cylindrical inner boundary at $r = r_i$ with the external curved boundary fixed (zero displacement) viewed in the x, y' plane after transformation to elliptic coordinate system $\{\xi, \eta\}$ for (a) radially diverging waves and (b) converging waves with isotropic material properties.

harmonic shear wave motion in the phantom material is to apply motion of amplitude u_{zr_i} in the z direction using this cylindrical rod: $u_z[r = r_i, t] = \text{Real}[u_{zr_i} e^{j\omega t}]$. Henceforth, the fact that the *real* part is of interest will be implicit.

For an *isotropic* and homogeneous material in such a configuration, the following theoretical solution governs steady state shear wave motion at any location $r_i < r < r_0$:

$$u_z[r, t] = u_{zr_i} \frac{J_0[k_s r] - \beta Y_0[k_s r]}{J_0[k_s r_i] - \beta Y_0[k_s r_i]} e^{j\omega t}, \quad \beta = \frac{J_0[k_s r_0]}{Y_0[k_s r_0]}. \tag{1}$$

Here k_s is the shear wave number. And for the case of radiating into an unbounded medium $r_i < r$ with $r_0 \to \infty$, we have the following:

$$u_z[r, t] = u_{zr_i} \frac{H_0^{(2)}[k_s r]}{H_0^{(2)}[k_s r_i]} e^{j\omega t}. \tag{2}$$

Here J_0 and Y_0 are the zeroth-order Bessel functions of the first and second kind, respectively. And $H_0^{(2)}$ is the Hankel function of the second kind (or Bessel function of the fourth kind), appropriate for outgoing (radially diverging) waves when using $e^{+j\omega t}$. This solution follows from the condition of axisymmetry established by the isotropic, homogeneous medium with symmetric (nonhomogeneous at r_i and homogeneous at r_0) boundary conditions, thus eliminating higher order Bessel functions that will have θ dependence.

In the case of *transverse isotropy* with the y axis parallel to the axis of isotropy (along the fiber axis), axisymmetry is destroyed and Eqs. (1) and (2) are no longer valid. Now consider a transformation to a new Cartesian coordinate system, with y replaced by $y' = y/\sqrt{1 + \phi}$ for a purely elastic case or for the case that the ratio of shear loss to storage moduli is the same in parallel and perpendicular directions: $\eta = \mu_{\perp I}/\mu_{\perp R} = \mu_{\parallel I}/\mu_{\parallel R}$. Here, shear anisotropy $\phi = \mu_{\parallel R}/\mu_{\perp R} - 1$. For the more general viscoelastic case when these ratios are not the same we will divide y by the ratio of shear wavelength along the fiber direction (parallel to the axis of isotropy) with respect to the shear wavelength perpendicular to the fiber direction (parallel to the plane of isotropy).

In this new coordinate system, shear waves propagating in the $\{x, y'\}$ plane polarized in the z direction will all propagate at the same phase speed, with the same wavelength at a given frequency, independent of the direction of propagation θ. In the transformed coordinate system, this shear wave behavior is isotropic. However, the same length distortion must be applied to the cylindrical boundary conditions at $r = r_i$ and $r = r_0$, which are now elliptic boundary conditions in the $\{x, y'\}$ coordinate system. Specifically, in order to create isotropy, for the case of elasticity and viscoelasticity with constant η, we are distorting space as a function of θ by reducing length by a factor of $\sqrt{1 + \phi \cos^2[\theta]}$ where θ denotes the angle of propagation with respect to the fiber axis. This is exactly an elliptic coordinate system.

We cannot satisfy the necessary distortion condition at both $r = r_i$ and $r = r_0$ simultaneously with a simple transformation to one elliptic coordinate system. For the unbound case with $r_0 \to \infty$, this is not a limitation, as we need only satisfy the distortion condition at $r = r_i$. For the bounded condition, we will work sequentially, first solving the unbounded diverging response using r_i to establish our new elliptic coordinate system, and then calculating the converging bounded reflection using r_0 to establish another elliptic coordinate system, summing these responses to satisfy the condition that $u_z[r_0, t] = 0$.

Shear wave motion propagating in the $\{x, y'\}$ plane with z polarization can be expressed in terms of angular and radial Mathieu functions[12,13] via a separation of variables approach to the governing partial differential equation, in a way analogous to how sinusoidal and Bessel functions are used to construct shear wave motion subject to a cylindrical boundary condition.[14] For the case of an unbounded medium we will consider a finite dimension rod at the origin of radius r_i and transform to elliptic coordinates $\{\xi, \eta\}$ such that $x = F\cosh[\xi]\cos[\eta]$ and $y' = F\sinh[\xi]\sin[\eta]$, where $F = r_i/\cosh[\xi_i] = (r_i/\sqrt{1+\phi})/\sinh[\xi_i]$ $0 \le \eta \le 2\pi$, $\xi_i \le \xi$. The coordinates $\{\xi, \eta\}$ and the distance from the origin to each focal point, F, are indicated in Fig. 1(a). The nonhomogeneous inner radius boundary condition is $u_z[\xi = \xi_i, t] = u_{zr_i}e^{j\omega t}$. The imposed uniform displacement on the elliptic inner boundary at $\xi = \xi_i$ allows only for Mathieu functions that have even parity with periodicity of π radians. Unlike in the case of cylindrical coordinates, there is no single member of the Mathieu function set that can satisfy this imposed nonhomogeneous symmetric inner boundary condition. The response for the outgoing wave, $u_{zH}[\xi, \eta]$, is given by

$$\frac{u_{zH}[\xi, \eta]}{u_{zH}[\xi_i, \eta]} = 2\sum_{n=0}^{\infty} A_0^{2n}[q]\frac{He_{2n}[\xi, q]}{He_{2n}[\xi_i, q]}ce_{2n}[\eta, q], \tag{3}$$

where $He_{2n}[\xi, q]$ is the radial (modified) even parity Hankel–Mathieu function of the second kind (also known as a radial Mathieu function of the fourth kind) and $ce_{2n}[z, q]$ is the angular even parity Mathieu function, all of periodicity π radians. And $\xi_i = \text{arctanh}[1/\sqrt{1+\phi}]$, $q = (Fk/2)^2$, and $k = \omega\sqrt{\rho/\mu}$. Here q is known as a Mathieu parameter and its value and that of F increase with the degree of shear anisotropy ϕ. For the isotropic case, both are zero and the angular and radial Hankel–Mathieu functions collapse to sinusoidal and Hankel functions, respectively, exactly matching isotropic theory. Equation (3) satisfies the inner boundary condition because we have from Eq. (28.11.3) of Wolf[15] the following:

$$1 = 2\sum_{n=0}^{\infty} A_0^{2n}[q]ce_{2n}[\eta, q]. \tag{4}$$

The coefficients $A_{2m}^{2n}[q]$ for $n = 0, 1, 2, \ldots$ and $m = 0, 1, 2, \ldots$ can be approximated based on solving an eigenvalue problem, which will have $n = 1, \ldots, N$ solutions for the eigenvalue a with $n = 1, \ldots, N$ corresponding eigenvectors of length N.[16]

Equation (3) can be used to calculate the steady state response of the outgoing wave at a distance $r = r_0$ at any angle θ by solving $u_{zH}[\xi, \eta]$ at values of ξ and η that correspond to $r = r_0$ for $0 \le \theta \le 2\pi$. These values will vary with θ but will have even parity with periodicity of π radians over the range $0 \le \theta \le 2\pi$. To identify the complete steady state solution a zero boundary condition at $r = r_0$ is needed. This will be achieved by adding a reflected radially converging wave $u_{zJ}[\xi, \eta]$ with a nonhomogeneous boundary condition at $r = r_0$ that is exactly the same amplitude but opposite in sign. The process of calculating this reflected radially converging wave is as follows.

We now transform to a new set of elliptic coordinates $\{\xi, \eta\}$ such that $x = F\cosh[\xi]\cos[\eta]$ and $y' = F\sinh[\xi]\sin[\eta]$, where $F = r_0/\cosh[\xi_0] = (r_0/\sqrt{1+\phi})/\sinh[\xi_0]$, $0 \le \eta \le 2\pi$, $\xi \le \xi_0$ [Fig. 1(b)]. The nonhomogeneous boundary condition at $\xi = \xi_0$, which has even parity with periodicity of π radians over the range $0 \le \theta \le 2\pi$ can be expressed in terms of a Fourier series as follows, where a_{2m} can be complex-valued to capture the in-phase and out-of-phase response:

$$u_{zH}[\xi_0, \eta] = \sum_{m=0}^{\infty} a_{2m}\cos[2m\eta]. \tag{5}$$

Furthermore, from Eq. (28.11.4) of Wolf[15] we have that

$$\cos[2m\eta] = \sum_{n=0}^{\infty} A_{2m}^{2n}[q]ce_{2n}[\eta, q]. \tag{6}$$

Given this, the reflected converging response $u_{zJ}[\xi,\eta]$ can be expressed as

$$u_{zJ}[\xi,\eta] = -\sum_{m=0}^{\infty} a_{2m}\left(\sum_{n=0}^{\infty} A_{2m}^{2n}[q]\,\frac{Je_{2n}[\xi,q]}{Je_{2n}[\xi_0,q]}\,ce_{2n}[\eta,q]\right). \tag{7}$$

Here, $Je_{2n}[\xi,q]$ is the radial (modified) even parity Mathieu function of the first kind and $ce_{2n}[z,q]$ is the angular even parity Mathieu function, all of periodicity π radians. And $\xi_0 = \text{arctanh}[1/\sqrt{1+\phi}]$, $q = (Fk/2)^2$, and $k = \omega\sqrt{\rho/\mu}$. Thus, the complete steady state response is

$$u_z[\xi,\eta] = u_{zH}[\xi,\eta] + u_{zJ}[\xi,\eta]. \tag{8}$$

However, note that $u_{zJ}[\xi,\eta]$ neglects the boundary condition created by the rod of radius r_i at the center. And, in fact, an additional outgoing reflection may need to be added to Eq. (8) to address this, and so forth, until reflections become negligible due to viscous attenuation of the response. The effect of this is explored in numerical simulations in Sec. 3.

Finally, while the summations in equations above are infinite, as n increases the magnitude of $A_{2m}^{2n}[q]$ significantly decreases such that the summation in n can be truncated. Likewise, Fourier series informs us that, as m increases, the magnitude of the terms will also approach zero and the summation in m can be truncated. In the results presented in Sec. 3 $N = M = 8$ were used. Increasing N or M further had a negligible effect.

3. Numerical validation case studies

The analytical approach described in Sec. 2 was implemented for specific case studies in MATLAB Version 16a (Mathworks Inc., Natick, MA) utilizing a free downloadable Mathieu function toolbox.[16] To validate the theoretical approach, predictions from it were compared to those from computational FEA.

The case study configuration is based on an experimental setup used by other groups to conduct Magnetic Resonance Elastography (MRE) on biological tissue and phantom material specimens, utilizing geometrically spreading (radially diverging) shear wave excitation, as summarized in Sec. 1. Geometry and physiologically-relevant material property values for the cases are provided in Table 1 and are consistent with values used in another study of geometrically focused (radially converging) wavefronts.[1] The theoretical solution assumes the cylinder has infinite height along its principle axis in the z direction. However, in the finite element (FE) model it is 20 mm in height, with the upper and lower surfaces having free boundary conditions. These finite boundary conditions coupled with the nonhomogeneous boundary condition of vertical oscillatory motion $u_{zr_i}e^{j\omega t}$ along the z axis result in standing Rayleigh–Lamb (RL) waves.[17,18] However, with the given dimensions, level of viscosity, and wavelengths the differences between these RL waves and shear waves in the infinite height cylinder are expected to be small.

Numerical FE studies using harmonic analysis were conducted using COMSOL Multiphysics Version 5.3a (COMSOL, Burlington, MA) software. The automatically meshed FE model contained 46 646 vertices, 266 724 quadratic tetrahedral elements (0.004 to 0.4 mm size), 9156 triangular elements, 379 edge elements, and 10 vertex elements. The minimum and average element quality was 0.19 and 0.66, respectively. The element volume ratio was 0.05325 and the mesh volume was 1004 mm^3. (Mesh resolution was decided upon when further increases had a negligible effect on the solution.) The outer curved boundary is fixed and a harmonic displacement is applied along the central axis, simulating a rod of infinitesimal radius oscillating axially in the center of the phantom.

Table 1. Geometrical and material parameter values for case study.

Parameter	Nomenclature	Value(s)
Cylinder outer radius	r_0	4 mm
Cylinder inner radius	r_i	0 (0.02) mm
Shear storage modulus in plane of isotropy	$\mu_{\perp R}$	2.77 kPa
Ratio of shear loss to storage moduli	$\eta = \frac{\mu_{\perp I}}{\mu_{\perp R}} = \frac{\mu_{\parallel I}}{\mu_{\parallel R}}$	0.15
Shear anisotropy	ϕ	1
Density	ρ	1000 $\frac{\text{kg}}{\text{m}^3}$
Frequency	f	1 kHz

Typical computation times for the single frequency harmonic analysis of this model was about 40 min using 64-bit operating system, ×64 based processor, Intel® Xeon® CPU E5-2609 0 with a clock speed of 2.40 GHz, and 256 GB RAM. Further description of the FE method used in this study can be found in Ref. 1. The analytical approach used to calculate the results presented below took about a second in MATLAB.

In Fig. 2 we see a comparison of the theoretical and FE solutions for the z displacement on an axial slice (x-y plane) with the displacement excitation for the material parameter values in Table 1. (For the theoretical solution we set $r_i = 0.02$ mm, which was comparable to element dimensions used in the FE model). Specifically, in Figs. 2(a) and 2(b) we see the in-phase and out-of-phase (with respect to the excitation) responses, respectively, for the diverging solution u_{zH}, based on Eq. (3). In Figs. 2(c) and 2(d) we see the in-phase and out-of-phase responses, respectively, for the complete solution u_z, based on Eq. (8). The steady state (harmonic analysis) FE solution, in-phase and out-of-phase, is shown in Figs. 2(e) and 2(f), respectively. In

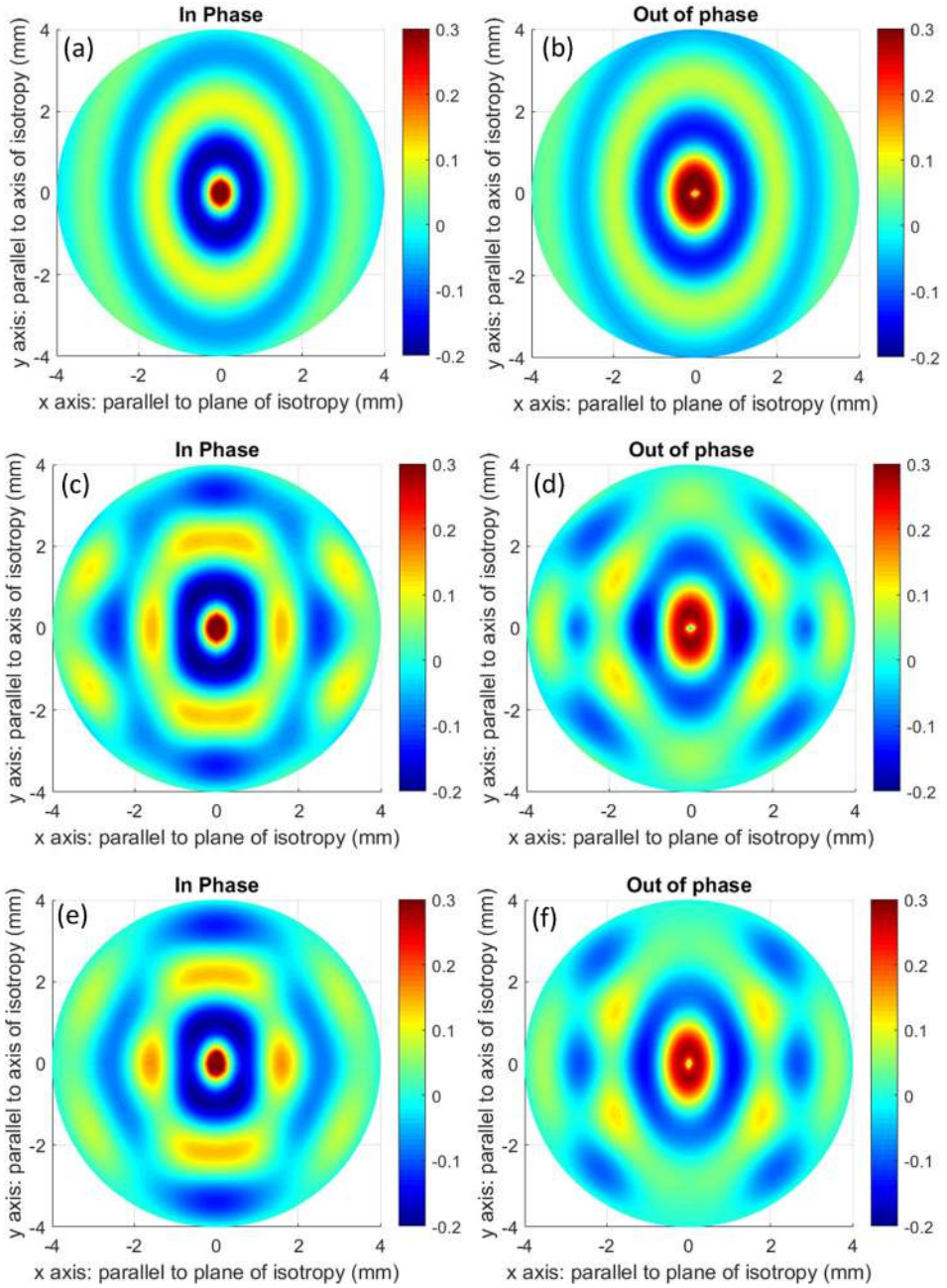

Fig. 2. (Color online) Normalized z direction displacement (u_{zr}/u_{zr_i}) on the x-y plane using the unbounded theoretical model [(a): in-phase, (b): 90° out-of-phase], using the bounded theoretical model [(c): in-phase, (d): 90° out-of-phase], and the transverse isotropic bounded FE numerical model [(e): in-phase, (f): 90° out-of-phase]. (See Ref. 19 for the supplementary material.)

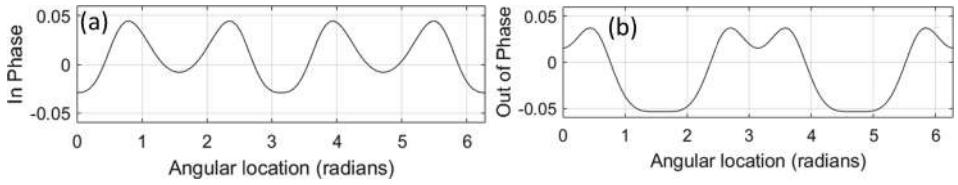

Fig. 3. Normalized z direction displacement (u_{zr}/u_{zr_i}) at $r_0 = 4$ mm in the x-y plane using the unbounded theoretical model u_{zH} [(a): in-phase, (b): 90° out-of-phase].

Figs. 3(a) and 3(b) the value of the diverging solution u_{zH} on the boundary $r_0 = 4\,\text{mm}$, which was "zeroed out" by introduction of u_{zJ}, is presented.

For the FE model the slice location is at the mid-height level (10 mm). In Fig. 4 line profiles of the complete theoretical and FE solutions within the slice in Fig. 2 and along the x and y axes, in-phase and out-of-phase, are plotted to provide a more direct comparison of the complete theoretical and numerical FE results. The percent difference along the x or y axis, $\Delta_x\%$ or $\Delta_y\%$, between theoretical and FE solutions is calculated for plots shown in Fig. 4 by taking the mean of the absolute values of the differences in the displacement profiles divided by the root-mean-square of the theoretical displacement profile.[1] These percent differences are provided in the figure captions.

4. Discussion

In all cases, there is expected to be some small level of error in the numerical FE simulation; it is an approximation. Additionally, neglecting the effect of finite boundaries on the top and bottom of the cylindrical phantom introduces a small amount of error into the theoretical solution. Both of these sources of error are thought to be independent of anisotropy. To quantify the combined effect of error in both the FE and theoretical approach independent of anisotropy, the case study of Sec. 3 but with $\phi = 0$ (isotropic case) was conducted. Percent differences between the FE and theoretical solutions were calculated the same way, with the theoretical solution now based on Eq. (1). Percent differences, in-phase and out-of-phase, were less than 2.5% and provide a target limit for accuracy in the anisotropic case.

For the anisotropic cases with $\phi = 1$, the primary source of additional error is believed to be the fact that the reflected wave, $u_{zJ}[\xi, \eta]$, does not account for the prescribed boundary condition at the center created by the rod. This is evident in the mismatch seen in the vicinity of x or $y = 0$ in Fig. 4. As noted below Eq. (8), this could be accounted for by adding an additional outgoing reflection to the overall solution in Eq. (8), in the same way the initial reflection $u_{zJ}[\xi, \eta]$ was added to have the overall solution match the zero boundary condition at r_0. Parametric studies (not shown) with both increased and decreased damping also supported this assessment in that, with decreased damping the error was greater, but with increased damping the error was reduced, as the reflected wave is further attenuated by the time it reaches the center of the cylinder.

The value used for damping, a ratio of shear loss to storage modulus of 0.15, is physiologically relevant;[5] so, for the application of interest we would not expect the damping level to differ drastically from this. And, while increased damping helps with the reflection issue, further increasing it combined with increased anisotropy amplifies

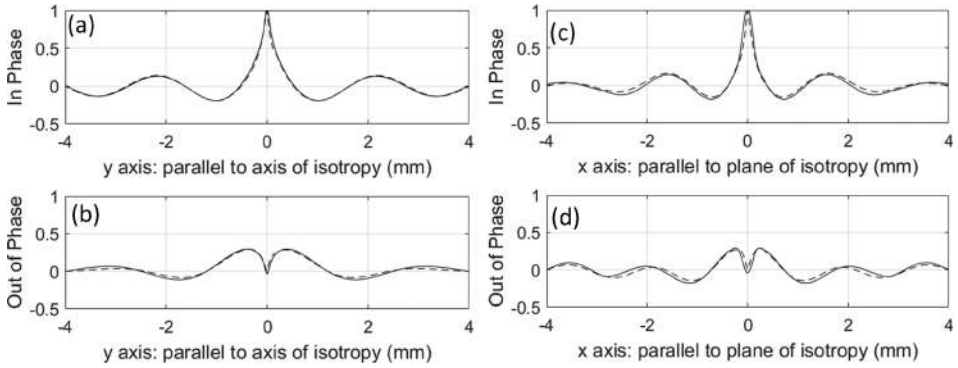

Fig. 4. Normalized z direction displacement (u_{zr}/u_{zr_i}) using the bounded theoretical model (solid line) and for the bounded FE numerical model (dashed line). (a) Along the y (fiber) axis in-phase: $\Delta_y = 5.2\%$; (b) along the y (fiber) axis 90° out-of-phase: $\Delta_y = 15\%$; (c) along the x axis in-phase: $\Delta_x = 15\%$; (d) along the x axis 90° out-of-phase: $\Delta_x = 23\%$.

a current limitation of the elliptic-based theoretical solution. As damping and anisotropy increase the imaginary part of q becomes larger, thereby increasing error in the algorithm used to calculate the Mathieu function coefficients $A_{2m}^{2n}[q]$ in Eqs. (3)–(8).

In documentation provided with the MATLAB functions that were adapted for this study,[16] it is noted that the algorithm is for positive and real values of q. But since q is proportional to the square of the shear wavenumber, which in turn is proportional to the reciprocal of the square root of the shear modulus μ, in the present application q will be complex-valued, since μ is complex-valued. Mathieu functions are defined and can be determined for complex-valued q, at least asymptotically.[15] However, a reliable algorithm for the values needed in the present study has not yet been found or developed by the authors.

Acknowledgments

Thanks to D. Nicholls for identifying helpful references on Mathieu functions. Funding from NIH Grant No. AR071162 is acknowledged.

References and links

[1]M. Guidetti and T. J. Royston, "Analytical solution for converging elliptic shear wave in a bounded transverse isotropic viscoelastic material with nonhomogeneous outer boundary," J. Acoust. Soc. Am. **144**, 2312–2323 (2018).

[2]Q. C. C. Chan, G. Li, R. L. Ehman, R. C. Grimm, R. Li, and E. S. Yang, "Needle shear wave driver for magnetic resonance elastography," Mag. Res. Med. **55**, 1175–1179 (2006).

[3]K. P. McGee, R. D. Hubmayr, D. Levin, and R. L. Ehman, "Feasibility of quantifying the mechanical properties of lung parenchyma in a small animal model using ^{1}H magnetic resonance elastography (MRE)," J. Mag. Res. Imag. **29**, 838–845 (2009).

[4]G. Li, J.-M. Liang, P.-W. Li, X. Yao, P. Z. Pei, W. Li, Q.-H. He, X. Yang, Q. C. C. Chan, P. Y. S. Cheung, Q. Y. Ma, S. K. Lam, P. Y. C. Cheng, and E. S. Yang, "Physiology and cell biology of acupuncture observed in calcium signaling activated by acoustic shear wave," Pflügers Archiv—Eur. J. Physiol. **462**, 587–597 (2011).

[5]J. L. Schmidt, D. J. Tweten, A. N. Benegal, C. H. Walker, T. E. Portnoi, R. J. Okamoto, J. R. Garbow, and P. V. Bayly, "Magnetic resonance elastography of slow and fast shear waves illuminates differences in shear and tensile moduli in anisotropic tissue," J. Biomech. **49**, 1042–1049 (2016).

[6]R. J. Okamoto, E. H. Clayton, and P. V. Bayly, "Viscoelastic properties of soft gels: Comparison of magnetic resonance elastography and dynamic shear testing in the shear wave regime," Phys. Med. Biol. **56**, 6379–6400 (2011).

[7]P. F. Beauchemin, P. V. Bayly, J. R. Garbow, J. L. S. Schmidt, R. J. Okamoto, F. Chériet, and D. Périé, "Frequency-dependent shear properties of annulus fibrosus and nucleus pulposus by magnetic resonance elastography," NMR Biomed. **E3918**, 1–8 (2018).

[8]P. V. Bayly and J. R. Garbow, "Pre-clinical MR elastography: Principles, techniques, and applications," J. Mag. Res. **291**, 73–83 (2018).

[9]S. Chatelin, M. Bernal, T. Deffieux, C. Papadacci, P. Flaud, A. Nahas, C. Boccara, J.-L. Gennisson, M. Tanter, and M. Pernot, "Anisotropic polyvinyl alcohol hydrogel phantom for shear wave elastography in fibrous biological soft tissue: A multimodality characterization," Phys. Med. Biol. **59**, 6923–6940 (2014).

[10]M. Wang, B. Byram, M. Palmeri, N. Rouze, and K. Nightingale, "Imaging transverse isotropic properties of muscle by monitoring acoustic radiation force induced shear waves using a 2-D matrix ultrasound array," IEEE Trans. Med. Imaging **32**, 1671–1684 (2013).

[11]J. L. Gennisson, T. Deffieux, M. Fink, and M. Tanter, "Ultrasound elastography: Principles and techniques," Diagnostics Intervent. Imag. **94**, 487–495 (2013).

[12]J. C. Gutiérrez-Vega, R. M. Rodríguez-Dagnino, M. A. Meneses-Nava, and S. Chávez-Cerda, "Mathieu functions, a visual approach," Am. J. Physics **71**, 233–242 (2003).

[13]S. M. Hasheminejad and A. Ghaheri, "Free vibration analysis of a finite-length isotropic solid elliptic cylinder using exact three dimensional elasticity theory," Appl. Math. Model. **37**, 8725–8741 (2013).

[14]K. Graff, *Wave Motion in Elastic Solids* (Dover, New York, 1991).

[15]G. Wolf, "Chapter 28 Mathieu Functions and Hill's Equation," in *Digital Library of Mathematic Functions, Version 1.0.18* (National Institute of Standards and Technology, March 27, 2018).

[16]E. Cojocaru, "Mathieu functions computational toolbox implemented in Matlab," Mathieu Functions Toolbox v. 1.0 arXiv:0811.1970v2 (2008).

[17]F. C. Meral, T. J. Royston, and R. L. Magin, "Rayleigh-Lamb wave propagation on a fractional order viscoelastic plate," J. Acoust. Soc. Am. **129**, 1036–1045 (2011).

[18]S. Brinker, S. P. Kearney, T. J. Royston, and D. Klatt, "Simultaneous magnetic resonance and optical elastography acquisitions: Comparison of displacement images and shear modulus estimations using a single vibration source," J. Mech. Behav. Biomed. Mater. **84**, 135–144 (2018).

[19]See supplementary material at https://doi.org/10.1121/1.5088028 for animations of the unbounded and bounded analytical models and bound FEA displacements, respectively, through a complete phase cycle.